# Multiscale Simulations of 2-D Material Ink-Based Printed Network Devices

Prabhat Kumar Dubey, Damiano Marian, and Gianluca Fiori, *Senior Member, IEEE*

***Abstract*— We present a simulation study of printed transistors composed of networks of two-dimensional materials flakes based on a multiscale approach. Printed devices are modeled by generating flake distribution using a Monte Carlo method, performing ab initio density functional theory (DFT) and nonequilibrium Green's function (NEGF) calculations to obtain flake-to-flake mobility and finally computing transport in a three-dimensional drift-diffusion scheme coupled with the electrostatics by means of the Poisson equation. The method has been applied to $MoS_2$-based devices while investigating the impact of trap charges on the device performances as well as the mixing of $MoS_2$with graphene, a technological option currently experimentally investigated in the literature. We will show that the presence of traps is detrimental to the OFF current, which could be the main reason for the reduced current modulation observed in experiments. Mixing $MoS_2$with graphene can instead be considered as an option to optimize the ON and OFF current of the device.**

***Index Terms*— 2-D materials, multiscale simulation, network devices, printed transistors.**

## I. Introduction

THE demand for low-power flexible electronics is growing due to the emergence of modern technologies such as the Internet of Things [1], flexible, and smart electronics [2], [3], where printable electronics could play its role as enabling technology. Traditionally, organic polymers have been the leading semiconductor material for printing of devices such as light-emitting diodes (LEDs), photodetectors, and transistors [4], [5], [6], [7], [8], [9], but they are encountering some limitations regarding the achievable mobility, the stability, and the cost [10]. The 2-D materials represent an alternative option due to their unique features demonstrated so far, such as their high mobility, good ON–OFF ratio, atomic thickness, transparency, and flexibility [11]. Many experimental demonstrations of 2-D material-based printed devices have been recently reported [12], [13], [14], [15], [16], [17], [18], [19], [20], [21], [22].

While in recent years, a lot of efforts have been performed in order to demonstrate the potential of this technology from an experimental point of view, a theoretical investigation of the main physical mechanisms at play in 2DM-printed devices has been so far scarcely addressed. A multiscale method has been recently presented in [23] by some of the authors in order to simulate transport in printed network based on the same type of 2-D material flakes, which has been validated against experimental results.

In the present work, we are further extending the model considering also the impact of nonidealities such as the presence of trap states and including the possibility of having mix of different inks, with a focus on the device electrical behavior and the physical effects affecting the performance of fabricated devices. Trap states have been indeed argued to be a dominating factor for carrier transport in $MoS_2$ network devices [12] and $MoS_2$–graphene composite ink has been used to optimize the performances of the printed devices, as demonstrated experimentally in [20] and [24].

Here, we will show that trap states severely affect printed device performances, and in particular, they degrade the ON/OFF current ratio of the device while reducing the capability of the gate to modulate the source-to-drain current ($I_{DS}$): this observation is consistent with the experimental results reported in [12]. While analyzing the impact of mixing graphene with $MoS_2$ ink, in order to optimize the device performance, we observe that below the percolation threshold of graphene network (i.e., transport is through both $MoS_2$ and graphene), the drain current depends on the Schottky barrier (SB) height at the $MoS_2$–graphene junction. We also notice that the addition of graphene ink increases the OFF current and reduces the ON/OFF ratio of the device. These observations are in line with the experimental observations presented in [22].

This article is organized into five sections. In Section II, we present the adopted modeling and simulation approach. The performance of $MoS_2$ network-based devices and the impact of trap states are reported in Section III. In Section IV, we investigate the mixed $MoS_2$–graphene ink-based transistor performance. Finally, we draw the conclusion in Section V.

## II. Device Structure and Simulation Approach

The device structure considered in this work is presented schematically in Fig. 1. It consists of a channel composed of a randomly generated network of two-dimensional $MoS_2$ flakes separated from the metal back gate by an oxide with a dielectric constant equal to three (a typical value for hBN [25]) and a thickness ($t_{ox}$) of 10 nm. The channel length ($L$) and width ($W$) are kept fixed at 3 and 1 $\mu$m, respectively [see Fig. 1(a)], while the thickness is 50 nm. In the generated

Manuscript received 25 October 2022; revised 8 December 2022; accepted 19 December 2022. Date of publication 6 January 2023; date of current version 24 January 2023. This work was supported in part by the European Project ERC PEP2D under Contract 770047, in part by WASP under Contract 825213, and in part by the Crosslab Department of Excellence Project. The review of this article was arranged by Editor M. A. Pavanello. *(Corresponding author: Prabhat Kumar Dubey.)*

The authors are with the Dipartimento di Ingegneria dell'Informazione, Università di Pisa, 56126 Pisa, Italy (e-mail: prabhat.dubey@ing.unipi.it; damiano.marian@gmail.com; gfiori@mercurio.iet.unipi.it).

Color versions of one or more figures in this article are available at https://doi.org/10.1109/TED.2022.3232082.

Digital Object Identifier 10.1109/TED.2022.3232082

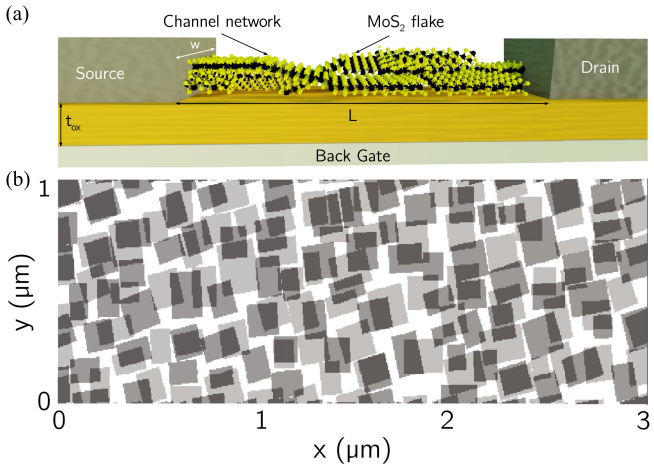


Fig. 1. (a) Sketch of $MoS_2$ printed network device, with indicated the main geometrical parameters. (b) Top view of a typical simulated network of $MoS_2$ flakes for FF = 0.7 showing a cross section of the distribution of two adjacent planes of flakes with an average dimension of 150 nm [21].

networks, we have considered flakes of lateral dimension of 150 nm on average as reported experimentally in [21]. The current flows between source and drain metal contacts through the $MoS_2$ network-based channel region.

The device structure is simulated using the multiscale simulation approach reported in [23], which consists of three main ingredients: 1) generation of a random distribution of flakes; 2) definition of the out-of-plane mobility; and 3) solution of transport through a drift-diffusion approximation. The first ingredient consists in generating a random distribution of flakes, with the possibility of arbitrarily setting the orientation, dimension, and overlap between flakes, using a Monte Carlo method [see Fig. 1(b)]. The second ingredient is aiming at connecting the diffusive (in-plane) transport along the flake with the ballistic (out-of-plane) vertical transport between the flakes. For this, we model the out-of-plane-to-in-plane conductance ratio by means of density functional theory (DFT) calculations, as presented in Figs. 2 and 3, and the Wannierization of the structure [26], which is used to perform transmission calculations within the nonequilibrium Green's function (NEGF) formalism implemented in the NanoTCAD ViDES software [23], [27]. This procedure is used to define the out-of-plane mobility, which is finally exploited, as the last ingredient, to solve the 3-D drift-diffusion equation self-consistently with the Poisson equation to calculate the current through the device (more details on the general framework of the method used can be found in [23]).

The impact of ink properties has been considered by a synthetic factor, which we refer as the filling factor (FF) parameter, defined as the ratio of the volume occupied by the flakes to the total volume of the channel [23]. This parameter, which aims at mimicking the compactness of the network structure, depends on the ink concentration, viscosity, and the number of print passes as well as on the post-annealing process.

The impact of trap states is taken into account considering a uniform distribution on the $MoS_2$ flakes along the channel. The traps are included while solving the Poisson and continuity

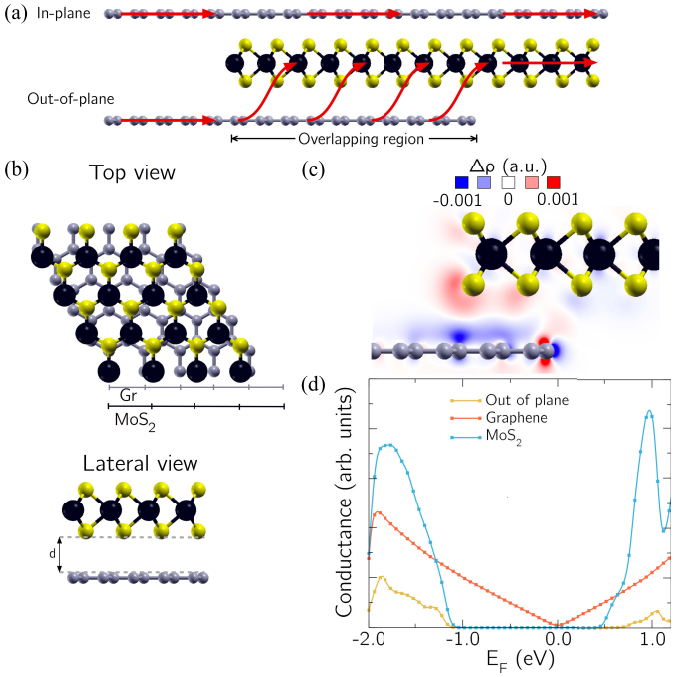


Fig. 2. (a) Schematic of the in-plane (top) and out-of-plane (bottom) transport. (b) Top and lateral views of $MoS_2$–graphene supercell structure for DFT calculations. (c) Charge density difference a partially overlapped structures of $MoS_2$–graphene. (d) In-plane conductance of graphene and $MoS_2$ flakes and average value of the out-of-plane conductance for three different values of the overlapping region (7.7, 10.2, and 12.8 nm) as a function of Fermi energy.

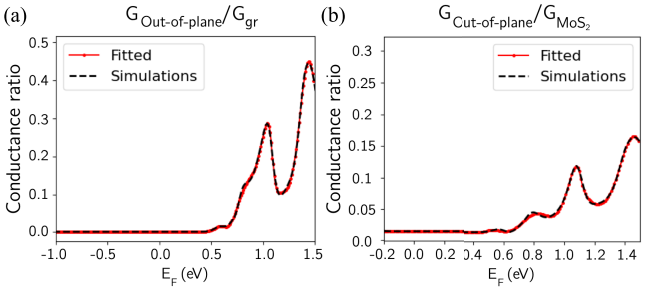


Fig. 3. Empirical curve fitting of DFT simulation results for conductance ratio. (a) Graphene-to-$MoS_2$ out-of-plane/graphene-in-plane conductance. (b) $MoS_2$-to-graphene out-of-plane/$MoS_2$-in-plane conductance.

equations self-consistently, considering a Gaussian distribution in the bandgap of $MoS_2$

$$D(E) = D_{\text{it}} \exp\left(\frac{-(E - E_0)^2}{2E_k^2}\right) \tag{1}$$

where $D_{\text{it}}$ is the concentration of trap states, $E_0 = 0.5$ eV is the center, and $E_k = 8$ kT is the variance of the Gaussian distribution. The values of $E_0$ and $E_k$ have been calculated using DFT results that are consistent with [28], [29]. We have simulated a set of 20 devices, each with a different random flake distribution, and two different values of FF, i.e., 0.4 and 0.7, to understand both the role of FF and trap states. The two values for the FF have been considered as the reference values corresponding to the case of not annealed and annealed networks since the annealing process provides more compact

networks in the channel region that increases the FF from 0.4 to a value of 0.7 [23].

The effect of mixing $MoS_2$ ink with graphene ink is modeled by extending and generalizing the procedure developed for the homo-material junctions in [23]. In particular, the in-plane and out-of-plane mobility, i.e., the transport within a flake (that can be either $MoS_2$ or graphene) or between two partially overlapped flakes can significantly differ [see Fig. 2(a)]. In order to consider this anisotropy, we perform the following multiscale procedure. First, we define a bilayer heterostructure of graphene and $MoS_2$, consisting of four elementary cells of $MoS_2$ and five elementary cells of graphene, in order to commensurate the two materials [see Fig. 2(b)]. We then perform DFT calculations of the structure exploiting the Quantum Espresso suite [30] and extract the Wannier Hamiltonian through the Wannier90 code [26]. Furthermore, we construct an extended Hamiltonian, which allows computing the in-plane transmission, i.e., isolated graphene or $MoS_2$ flake (see Fig. 2(a) top), and the out-of-plane transmission, i.e., from one material to the other (see Fig. 2(a) bottom), varying the overlapping region from 7.7 to 12.8 nm, in NanoTCAD ViDES [27] (see [31] for more details on how the extended Hamiltonian is constructed from the bilayer Wannier Hamiltonian). It is worth observing that the transmission between the flakes, in the out-of-plane case, occurs mainly at the edges of the flakes, being almost independent of the specific overlapping region [31]. To confirm this, in Fig. 2(c), we report the charge density difference for the heterostructure, calculated as $\Delta\rho = \rho_{\text{hetero}} - \rho_{MoS_2} - \rho_{\text{gr}}$, where $\rho_{\text{hetero}}$ is the charge of the heterostructure and $\rho_{MoS_2}$ and $\rho_{\text{gr}}$ are the charges of the $MoS_2$ and the graphene flakes alone, respectively. The charge density difference illustrates the distribution of the charges of the heterostructure with respect to the single flake case: we can observe that the main difference is localized at the edges of the flakes and tends to vanish far from the overlapping region [30].

From the in-plane and out-of-plane transmissions, we compute the in-plane conductance of graphene $[G_{\text{gr}}(E_F)]$ and $MoS_2$ $[G_{MoS_2}(E_F)]$ and the out-of-plane conductance $[G_{\text{out-of-plane}}(E_F)]$, considering the average transmission for the different overlapping regions considered [see Fig. 2(d)]. Finally, we obtain the conductance ratio (out-of-plane/in-plane), which we assume to be directly proportional to the mobility ratio, for both graphene ($g_{\text{gr}}(E_F) = G_{\text{out-of-plane}}/G_{\text{gr}}$) and $MoS_2$ ($g_{MoS_2}(E_F) = G_{\text{out-of-plane}}/G_{MoS_2}$) as a function of the Fermi energy. We did empirical curve fitting to find the energy-dependent expression for the conductance ratio for a carrier from graphene-to-$MoS_2$ ($g_{\text{gr}}$) in Fig. 3(a) and from $MoS_2$-to-graphene ($g_{MoS_2}$) in Fig. 3(b).

In Appendix A, we report the details of the curve fitting shown in Fig. 3(a) and (b). These expressions are then used to model the energy-dependent mobility for interflake transport regions extending the procedure reported in [23] as follows. We have considered a fixed in-plane mobility for $MoS_2$ and graphene, respectively, $\mu_{\text{gr}} = 200$ cm$^2$/Vs and $\mu_{MoS_2} = 2$ cm$^2$/Vs, while the energy-dependent out-of-plane mobility

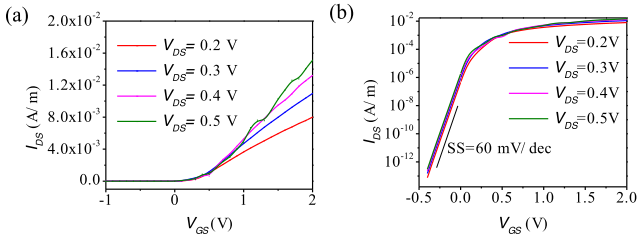


Fig. 4. Transfer characteristics of $MoS_2$ ink-based printed network device on (a) linear scale and (b) semilog scale for different $V_{DS}$'s.

at the interface between graphene and $MoS_2$ is taken as

$$\mu_{\text{out-of-plane}}(E_F) = \frac{1}{2}\left[g_{\text{gr}}(E_F)\cdot\mu_{\text{gr}} + g_{MoS_2}(E_F)\cdot\mu_{MoS_2}\right] \tag{2}$$

i.e., defined as the weighted average of the in-plane mobilities on the conductance ratios for graphene and $MoS_2$. The $MoS_2$-to-$MoS_2$ and graphene-to-graphene out-of-plane mobility is modeled according to [23].

It is worth underlining that the carrier concentration and the in-plane and out-of-plane transport are solved self-consistently considering the potential and the quasi-Fermi level at each iterative solution. Indeed, both the charge in the $MoS_2$ (graphene) flakes and the out-of-plane mobility depend on the potential and the quasi-Fermi level, thus properly coupling the 3-D electrostatics and the interflake transport. The model and the parameters used in the simulations have been validated in [23] showing very good agreement with experimental results [19], [32].

## III. Result and Discussion

The transfer characteristics of the $MoS_2$ network device (as in Fig. 1) in the ideal case (i.e., without defects) are presented in Fig. 4. In the absence of trap states, the device characteristics show a large $I_{\text{ON}}/I_{\text{OFF}}$ ratio and a subthreshold swing (SS) of 60 mV/decade. In order to appreciate the complexity of transport in printed devices in Fig. 5, we report the cross section of the in-plane, source-to-drain (a), and the out-of-plane, bottom-to-top (b), current components. It can be observed that in-plane transport is unidirectional from source to drain, and on the other hand, the out-of-plane current has both positive, from bottom to top, and negative, from top to bottom, components.

It has been observed experimentally that the drain current in $MoS_2$ ink-based printed network devices hardly modulates with the gate voltage ($V_{\text{GS}}$) [12]. The reason behind this effect could be the large number of defects present in printed 2-D material-based devices (either at the edges or within the flakes). To get insight on this phenomenon, we have investigated the impact of defects on the performance of the device, considering the distribution reported in (1). Considering the randomness of flake distribution and their arrangement, we have generated 20 different networks for each value of $D_{\text{it}}$ and FF. In Fig. 6(a), the computed transfer characteristics are shown for an FF of 0.4 and for different trap densities ($D_{\text{it}}$).

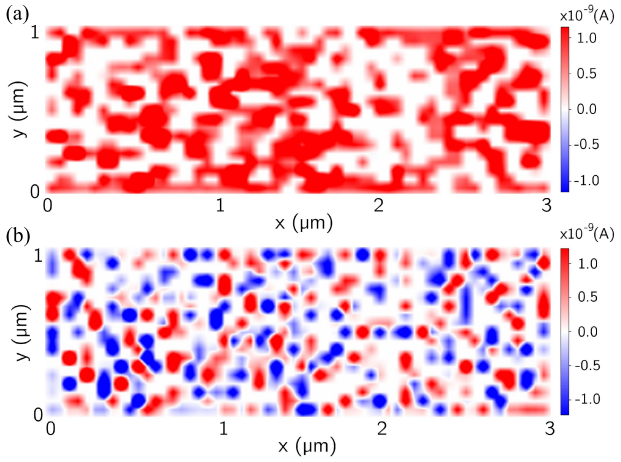


Fig. 5. Cross section of the current in $MoS_2$ network device for FF = 0.7 at $V_{GS}$ = 1 V: (a) in-plane (*x*-direction) source-to-drain current and (b) out-of-plane (*z*-direction) bottom-to-top current.

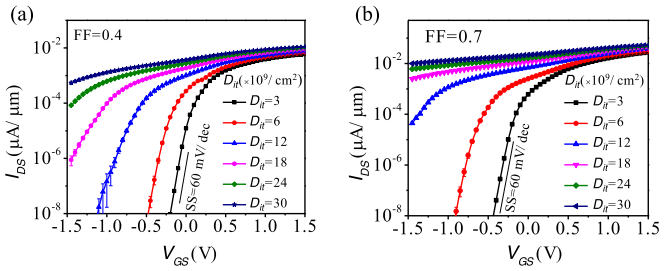


Fig. 6. Impact of trap density ($D_{it}$) on the transfer characteristics of $MoS_2$-based network devices for (a) FF = 0.4 and (b) FF = 0.7 and $V_{DS}$ = 0.3 V.

It can be observed that the OFF current increases with the trap density ($D_{it}$). This results in a very low ON/OFF ratio for the studied device, which is in line with the experimental result observed in [12], where a weak current modulation with $V_{GS}$ has been observed. The impact of trap charges on transfer characteristics corresponding to an FF of 0.7 is presented in Fig. 6(b). It can be observed that like Fig. 6(a), the OFF current and subthreshold slope of the device increase while increasing the trap density, thus reducing the ON/OFF current ratio of the devices. Furthermore, we observe that the conductivity of the channel increases with the FF due to the increasing number of conducting paths. The observations suggest that postprocessing annealing is not improving the performance in terms of current modulation (assuming that post-annealing is not healing the channel from defects).

## IV. $MoS_2$–Graphene Composite Ink-Based FETs

The $MoS_2$-based network devices suffer by reduced mobility due to interflake transmissions. On the other hand, graphene inks show metallic conductivity due to higher electron mobility. This property of graphene can be exploited to enhance the mobility of $MoS_2$ network devices by mixing the $MoS_2$ ink with graphene ink as suggested in [22]. In this section, we investigate the $MoS_2$–graphene composite ink-based printed network devices [see Fig. 7(a)]. In the simulations, we have generated random $MoS_2$ and graphene flakes of average length 150 nm in a Monte Carlo fashion, as schematically shown in Fig. 7(b). Next, we define

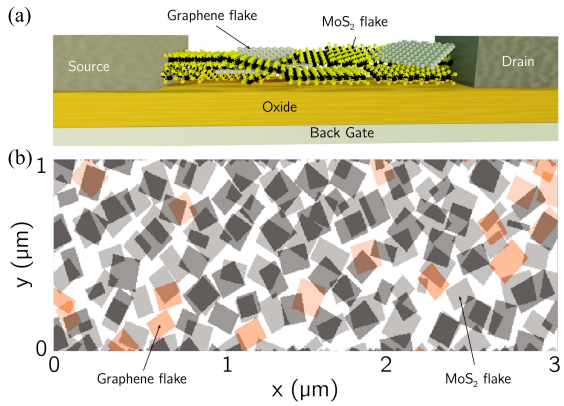


Fig. 7. (a) Schematic of $MoS_2$–graphene composite network randomly generated using the Monte Carlo scheme and (b) top view of the cross section of two adjacent planes of a typical simulated network of graphene–$MoS_2$ composite ink for FF = 0.7 with 10% graphene and average flake dimension of 150 nm [21].

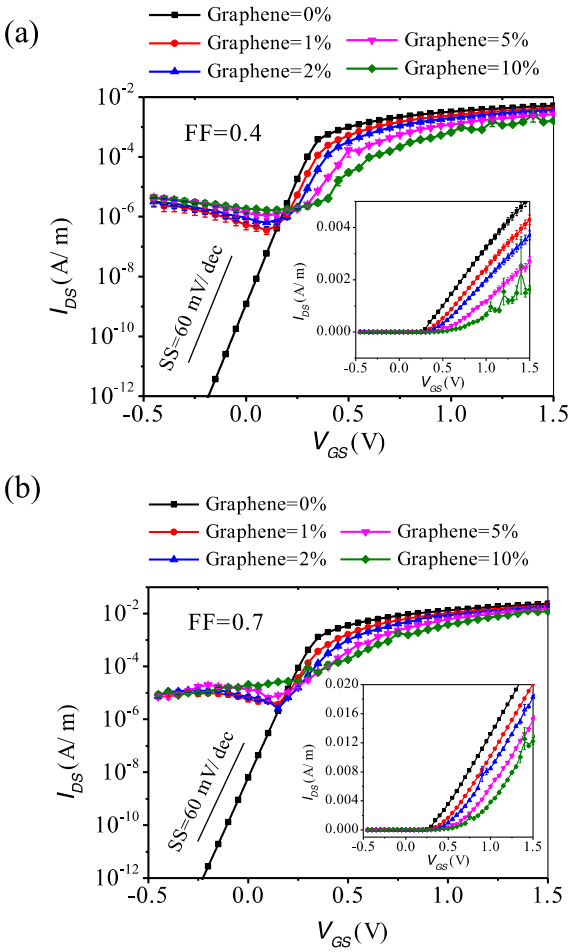


Fig. 8. Transfer characteristics of $MoS_2$–graphene composite ink-based printed device for SB of 0.5 eV. (a) FF = 0.4. (b) FF = 0.7.

the mobility in both graphene and $MoS_2$ flakes along with interflake mobility as detailed in Section II. Also, for these simulations, we have considered 20 different networks for each value of FF and graphene percentage.

Fig. 8 shows the transfer characteristics of $MoS_2$ network devices with different percentages of graphene for two FFs (0.4 and 0.7). It can be observed from Fig. 8 that the device

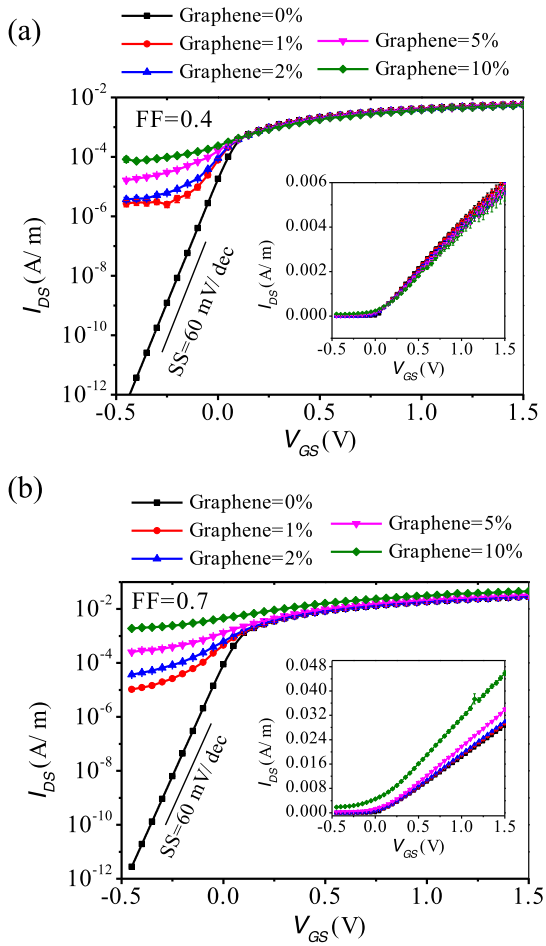


Fig. 9. Transfer characteristics of $MoS_2$–graphene composite ink-based printed transistor with $MoS_2$–graphene SB height of 0.25 eV. (a) FF = 0.4. (b) FF = 0.7.

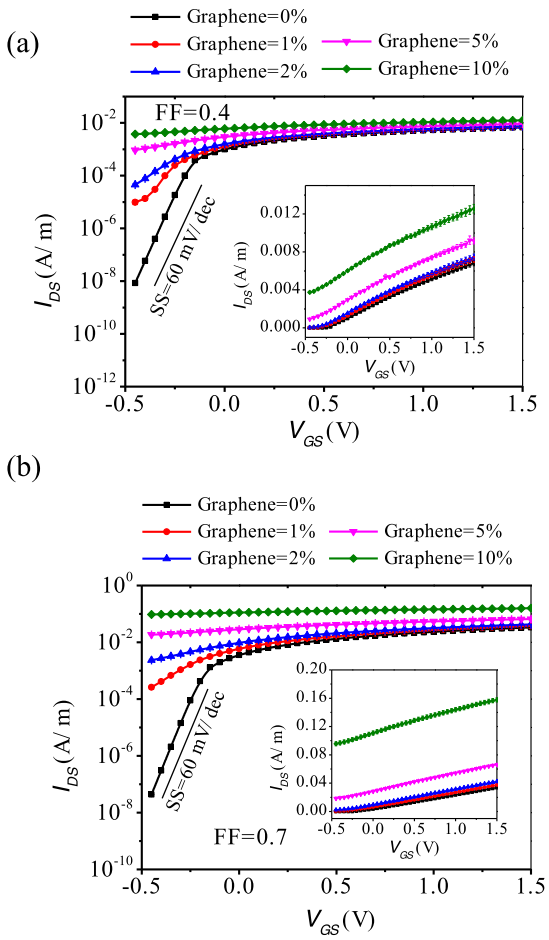


Fig. 10. Transfer characteristics of $MoS_2$–graphene composite ink-based printed transistor with $MoS_2$–graphene SB height of 0.0 eV. (a) FF = 0.4. (b) FF = 0.7.

ON current (and the conductance) reduces as the graphene percentage increases from 0% to 10%, which is counterintuitive and in disagreement with [22]. The reason for the observed effect can be related to the presence of a Schottky junction between $MoS_2$ and graphene flake, whose barrier height has been set to 0.5 eV as from our DFT simulation results (see Fig. 2(d) and [30]). However, while a Schottky junction may indeed be present at the flake interface, the exact value of the barrier may be difficult to be determined, due to the presence of nonidealities (e.g., defects) that may lead to a different picture as that drawn by DFT calculations. To understand, how sensitive are the results with respect to the assumed barrier height, we have considered two different values for the SB between $MoS_2$ and graphene flakes and, in particular, equal to 0.25 eV (see Fig. 9) and 0 eV (see Fig. 10). It can be observed that indeed, the conductivity of the $MoS_2$–graphene composite ink improves as the SB height is reduced. From Figs. 8 and 9, it is also clear that the increase of graphene percentage is leading to a degradation of the OFF current, due to the increasing number of conducting graphene paths between the reservoirs, which cannot completely switched OFF by the external electric field: a tradeoff between improved conductivity and preservation of OFF current and *SS* has then to be found when mixing $MoS_2$ with graphene.

## V. Conclusion

A multiscale simulation approach has been presented to investigate the performance of 2-D material ink-based (specifically $MoS_2$ and $MoS_2$–graphene composite ink) printed devices. The approach is general and can be used to investigate 2-D-printed devices with different materials. The results show that by adding graphene ink in $MoS_2$, the ON current can be improved at the cost of degrading the ON/OFF ratio. The developed model can also consider the impact of trap states on the device performance, which may explain the experimentally reported weak modulation of drain current on gate voltage of $MoS_2$ ink-based network FETs.

## Appendix A

The curve in Fig. 3(a) is fit as in the following, with a piecewise function:

$$G_{\text{gr-MoS2}} = 1 \times 10^{-4}, \quad \text{for} \quad -2 < E_F < 0.4 \tag{A1}$$

$$G_{\text{gr-MoS2}} = a_1x^6 + b_1x^5 + c_1x^4 + d_1x^3 + e_1x^2 + f_1x + g_1 \quad \text{for,} \quad 0.4 \le E_F \le 0.6 \tag{A2}$$

$$G_{\text{gr-MoS2}} = a_2x^6 + b_2x^5 + c_2x^4 + d_2x^3 + e_2x^2 + f_2x + g_2 \quad \text{for,} \quad 0.6 < E_F \le 1.1 \tag{A3}$$

$$G_{\text{gr-MoS2}} = a_3x^6 + b_3x^5 + c_3x^4 + d_3x^3 + e_3x^2 + f_3x + g_3 \quad \text{for} \quad 1.1 < E_F \le 1.5 \tag{A4}$$

TABLE I
FITTING PARAMETERS FOR GRAPHENE-TO-$MoS_2$ CONDUCTANCE

| Parameter | Value | Parameter | Value | Parameter | Value |
|---|---|---|---|---|---|
| $a_1$ | 7.63 $eV^{-6}$ | $a_2$ | -1644.71 $eV^{-6}$ | $a_3$ | 5340.61 $eV^{-6}$ |
| $b_1$ | -5761.74 $eV^{-5}$ | $b_2$ | 7977.88 $eV^{-5}$ | $b_3$ | -41970.25 $eV^{-5}$ |
| $c_1$ | 7329.59 $eV^{-4}$ | $c_2$ | -15972.32 $eV^{-4}$ | $c_3$ | 136983.74 $eV^{-4}$ |
| $d_1$ | -4914.98 $eV^{-3}$ | $d_2$ | 16889.49 $eV^{-3}$ | $d_3$ | -237702.19 $eV^{-3}$ |
| $e_1$ | 1834.42 $eV^{-2}$ | $e_2$ | -9945.36 $eV^{-2}$ | $e_3$ | 231321.39 $eV^{-2}$ |
| $f_1$ | -361.70$eV^{-1}$ | $f_2$ | 3091.69 $eV^{-1}$ | $f_3$ | -119716.69 $eV^{-1}$ |
| $g_1$ | 29.46 | $g_2$ | -396.41 | $g_3$ | 25745.66 |

TABLE II
FITTING PARAMETERS FOR $MoS_2$-TO-GRAPHENE CONDUCTANCE

| Parameter | Value | Parameter | Value |
|---|---|---|---|
| $\alpha_1$ | -768.40 $eV^{-7}$ | $\alpha_2$ | 425.91 $eV^{-7}$ |
| $\beta_1$ | 3957.73 $eV^{-6}$ | $\beta_2$ | -2952.32 $eV^{-6}$ |
| $\gamma_1$ | -8578.45 $eV^{-5}$ | $\gamma_2$ | 7735.30 $eV^{-5}$ |
| $\delta_1$ | 10139.54 $eV^{-4}$ | $\delta_2$ | -8275.10 $eV^{-4}$ |
| $\epsilon_1$ | -7056.87 $eV^{-3}$ | $\epsilon_2$ | -549.13 $eV^{-3}$ |
| $\theta_1$ | 2892.14 $eV^{-2}$ | $\theta_2$ | 9382.78 $eV^{-2}$ |
| $\zeta_1$ | -646.46 $eV^{-1}$ | $\zeta_2$ | -7973.08 $eV^{-1}$ |
| $\eta_1$ | 60.84 | $\eta_2$ | 2206.25 |

where *a, b, c, d, e, f,* and *g* are the fitting parameters with the values presented in Table I hereafter.

The curve in Fig. 3(b) is fit as

$$G_{\mathrm{MoS2-gr}} = 0.014, \quad \text{for}, \quad -2 < E_F < 0.45 \tag{A5}$$

$$G_{\mathrm{MoS2-gr}} = \alpha_1 x^7 + \beta_1 x^6 + \gamma_1 x^5 + \delta_1 x^4 + \epsilon_1 x^3 + \theta_1 x^2 + \zeta_1 x + \eta_1 \quad \text{for}, \quad 0.45 \le E_F \le 1.1 \tag{A6}$$

$$G_{\mathrm{MoS2-gr}} = \alpha_2 x^7 + \beta_2 x^6 + \gamma_2 x^5 + \delta_2 x^4 + \epsilon_2 x^3 + \theta_2 x^2 + \zeta_2 x + \eta_2 \quad \text{for}, \quad 1.1 < E_F \le 1.5 \tag{A7}$$

where, $\beta$, $\gamma$, $\delta$, $\epsilon$, $\theta$, $\zeta$, and $\eta$ are fitting parameters with the values presented in Table II hereafter.

## REFERENCES


[1] S. Li, L. Xu, and S. Zhao, "The Internet of Things: A survey," *Inf. Syst. Frontiers*, vol. 17, no. 2, pp. 243–259, 2015.

[2] S. Khan, L. Lorenzelli, and R. S. Dahiya, "Technologies for printing sensors and electronics over large flexible substrates: A review," *IEEE Sensors J.*, vol. 15, no. 6, pp. 3164–3185, Oct. 2015.

[3] R. Rayhana, G. G. Xiao, and Z. Liu, "Printed sensor technologies for monitoring applications in smart farming: A review," *IEEE Trans. Instrum. Meas.*, vol. 70, pp. 1–19, 2021.

[4] J. H. Burroughes et al., "Light-emitting diodes based on conjugated polymers," *Nature*, vol. 347, pp. 41–539, 1990.

[5] D. Zhu et al., "Organic donor-acceptor heterojunctions for high performance circularly polarized light detection," *Nature Commun.*, vol. 13, no. 1, p. 3454, Jun. 2022.

[6] Y. Yao, Y. Chen, H. Wang, and P. Samorì, "Organic photodetectors based on supramolecular nanostructures," *SmartMat*, vol. 1, no. 1, pp. 1–16, Dec. 2020.

[7] L.-L. Chua et al., "General observation of n-type field-effect behaviour in organic semiconductors," *Nature*, vol. 434, pp. 194–199, Mar. 2005.

[8] C. P. Jarrett, R. H. Friend, A. R. Brown, and D. M. Deleeuw, "Field effect measurements in doped conjugated polymer films: Assessment of charge carrier mobilities," *J. Appl. Phys.*, vol. 77, p. 6289, Feb. 1995.

[9] S. Conti, S. Lai, P. Cosseddu, and A. Bonfiglio, "An inkjet-printed, ultralow voltage, flexible organic field effect transistor," *Adv. Mater. Technol.*, vol. 2, no. 2, 2017, Art. no. 1600212.

[10] J. S. Chang, A. F. Facchetti, and R. Reuss, "A circuits and systems perspective of organic/printed electronics: Review, challenges, and contemporary and emerging design approaches," *IEEE J. Emerg. Sel. Topics Circuits Syst.*, vol. 7, no. 1, pp. 7–26, Mar. 2017.

[11] A. G. Kelly, D. Finn, A. Harvey, T. Hallam, and J. N. Coleman, "All-printed capacitors from graphene-BN-graphene nanosheet heterostructures," *Appl. Phys. Lett.*, vol. 109, no. 2, Jul. 2016, Art. no. 023107.

[12] J. Li, M. M. Naiini, S. Vaziri, M. C. Lemme, and M. Östling, "Inkjet printing of $MoS_2$," *Adv. Funct. Mater.*, vol. 24, pp. 6524–6531, Aug. 2014.

[13] A. G. Kelly et al., "All-printed thin-film transistors from networks of liquid-exfoliated nanosheets," *Science*, vol. 356, pp. 69–73, Apr. 2017.

[14] S. Conti et al., "Low-voltage 2D materials-based printed field-effect transistors for integrated digital and analog electronics on paper," *Nature Commun.*, vol. 11, no. 1, p. 3566, Jul. 2020.

[15] S. Lu et al., "Flexible, print-in-place 1D–2D thin-film transistors using aerosol jet printing," *ACS Nano*, vol. 13, no. 10, pp. 11263–11272, 2019.

[16] B. Li et al., "Inkjet-printed ultrathin $MoS_2$-based electrodes for flexible in-plane microsupercapacitors," *ACS Appl. Mater. Interfaces*, vol. 12, pp. 39444–39454, Aug. 2020.

[17] R. F. Hossain and A. B. Kaul, "Inkjet-printed $MoS_2$-based field-effect transistors with graphene and hexagonal boron nitride inks," *J. Vac. Sci. Technol. B*, vol. 38, no. 4, Jul. 2020, Art. no. 042206.

[18] I. Brunetti et al., "Inkjet-printed low-dimensional materials-based complementary electronic circuits on paper," *NPJ 2D Mater. Appl.*, vol. 5, no. 1, pp. 1–6, Nov. 2021.

[19] G. Calabrese et al., "Inkjet-printed graphene Hall mobility measurements and low-frequency noise characterization," *Nanoscale*, vol. 12, no. 12, pp. 6708–6716, 2020.

[20] E. Piatti et al., "Charge transport mechanisms in inkjet-printed thin-film transistors based on two-dimensional materials," *Nature Electron.*, vol. 4, no. 12, pp. 893–905, Dec. 2021.

[21] T. Carey et al., "Fully inkjet-printed two-dimensional material field-effect heterojunctions for wearable and textile electronics," *Nature Commun.*, vol. 8, no. 1, p. 1202, Oct. 2017.

[22] A. G. Kelly et al., "Tuneable photoconductivity and mobility enhancement in printed $MoS_2$/graphene composites," *2D Mater.*, vol. 4, no. 4, Sep. 2017, Art. no. 041006.

[23] M. Perucchini, D. Marian, E. G. Marin, T. Cusati, G. Iannaccone, and G. Fiori, "Electronic transport in 2D-based printed FETs from a multiscale perspective," *Adv. Electron. Mater.*, vol. 8, no. 5, May 2022, Art. no. 2100972.

[24] M. U. Jewel, F. Mokhtari-Koushyar, R. T. Chen, and M. Y. Chen, "All inkjet-printed high on/off ratio two-dimensional materials field effect transistor," in *Proc. IEEE 18th Int. Conf. Nanotechnol. (IEEE-NANO)*, Jul. 2018, pp. 1–4.

[25] S. Hong et al., "Ultralow-dielectric-constant amorphous boron nitride," *Nature*, vol. 582, pp. 511–515, Jun. 2020.

[26] A. A. Mostofi et al., "An updated version of wannier90: A tool for obtaining maximally-localised wannier functions," *Comput. Phys. Commun.*, vol. 185, pp. 2309–2310, Aug. 2014.

[27] *NanoTCAD ViDES*. Accessed: Apr. 20, 2021. [Online]. Available: http://vides.nanotcad.com/vides/

[28] M. H. Naik and M. Jain, "Substrate screening effects on the quasiparticle band gap and defect charge transition levels in $MoS_2$," *Phys. Rev. Mater.*, vol. 2, no. 8, Aug. 2018, Art. no. 084002.

[29] F. Fabbri et al., "Novel near-infrared emission from crystal defects in $MoS_2$ multilayer flakes," *Nature Commun.*, vol. 7, p. 13044, Oct. 2016.

[30] P. Giannozzi et al., "QUANTUM ESPRESSO: A modular and open-source software project for quantum simulations of materials," *J. Phys., Condens. Matter*, vol. 21, Sep. 2009, Art. no. 395502.

[31] E. Cannavò, D. Marian, E. G. Marín, G. Iannaccone, and G. Fiori, "Transport properties in partially overlapping van der Waals junctions through a multiscale investigation," *Phys. Rev. B, Condens. Matter*, vol. 104, no. 8, Aug. 2021, Art. no. 085433.

[32] D. McManus et al., "Water-based and biocompatible 2D crystal inks for all-inkjet-printed heterostructures," *Nature Nanotechnol.*, vol. 12, pp. 343–350, Jan. 2017.